Material-Dependent Implant Artifact Reduction Using SEMAC-VAT and MAVRIC

A Prospective MRI Phantom Study

Lukas Filli, MD, Lukas Jud, MD,* Roger Luechinger, PhD,† Daniel Nanz, PhD,* Gustav Andreisek, MD, MBA,‡§ Val M. Runge, MD,|| Sebastian Kozerke, PhD,† and Nadja A. Farshad-Amacker, MD**

Objective: The aim of this study was to compare the degree of artifact reduction in magnetic resonance imaging achieved with slice encoding for metal artifact correction (SEMAC) in combination with view angle tilting (VAT) and multiacquisition variable resonance image combination (MAVRIC) for standard contrast weightings and different metallic materials.

Methods: Four identically shaped rods made of the most commonly used prosthetic materials (stainless steel, SS; titanium, Ti; cobalt-chromium-molybdenum, CoCr; and oxidized zirconium, oxZi) were scanned at 3 T. In addition to conventional fast spin-echo sequences, metal artifact reduction sequences (SEMAC-VAT and MAVRIC) with varying degrees of artifact suppression were applied at different contrast weightings (T1w, T2w, PDw). Two independent readers measured in-plane and through-plane artifacts in a standardized manner. In addition, theoretical frequency-offset and frequency-offset-gradient maps were calculated. Interobserver agreement was assessed using intraclass correlation coefficient.

Results: Interobserver agreement was almost perfect (intraclass correlation coefficient, 0.86–0.99). Stainless steel caused the greatest artifacts, followed by CoCr, Ti, and oxZi regardless of the imaging sequence. While for Ti and oxZi rods scanning with weak SEMAC-VAT showed some advantage, for SS and CoCr, higher modes of SEMAC-VAT or MAVRIC were necessary to achieve artifact reduction. MAVRIC achieved better artifact reduction than SEMAC-VAT at the cost of longer acquisition times. Simulations matched well with the apparent geometry of the frequency-offset maps.

Conclusions: For Ti and oxZi implants, weak SEMAC-VAT may be preferred as it is faster and produces less artifact than conventional fast spin-echo. Medium or strong SEMAC-VAT or MAVRIC modes are necessary for significant artifact reduction for SS and CoCr implants.

Key Points:

- The amount of MR artifacts strongly depends on the prosthetic material.
- The effectiveness of SEMAC-VAT and MAVRIC depends on the prosthetic material and the contrast weighting.
- Stainless steel and cobalt-chromium-molybdenum require higher modes of SEMAC-VAT and MAVRIC compared with titanium or oxidized zirconium.

Key Words: magnetic resonance imaging, metal artifacts, implant materials, slice encoding for metal artifact correction, multiacquisition variable resonance image combination

(*Invest Radiol* 2017;52: 381–387)

Metal artifact reduction techniques in magnetic resonance imaging (MRI) are becoming progressively important given the increase in prosthetic procedures and thus the demand for postoperative imaging.[1,2] Magnetic resonance imaging allows visualization of soft tissue and osseous structures around metallic implants, for example, to detect periprosthetic fractures and complications.[3–6] However, metallic implants generate field inhomogeneities, signal voids, geometric distortion, and signal pileup, with more pronounced effects observed at higher field strength.[7,8]

Several techniques have been proposed to overcome these problems. Standard sequences can be optimized by using a higher bandwidth, shorter interecho intervals, shorter echo train length (ETL), and thinner slices.[6] In addition, dedicated techniques were developed such as view angle tilting (VAT), which reduces in-plane distortions but not through-plane artifacts.[9,10] Slice encoding for metal artifact correction (SEMAC) uses 2-dimensional slice selective excitations but then phase-encodes each slice in the through-plane dimension and combines them to form a composite image.[10–13] Multiacquisition variable resonance image combination (MAVRIC)[14] uses several 3-dimensional standard fast spin echo (FSE) images at different off-resonance frequencies and generates 1 combined image of the acquired data sets.[14,15] Recently, hybrids of these methods were introduced that are combinations of MAVRIC, VAT, or SEMAC.[10,16]

The amount of artifacts is known to depend on the type of metallic material as well as the contrast weighting.[8,17–19] Our hypothesis was that different scanning protocols are needed for different implant materials for artifact reduction. Thus, the purpose of this study was to compare the degree of artifact reduction with SEMAC-VAT and MAVRIC to determine optimal metal- and contrast-specific scan protocols.

MATERIALS AND METHODS

Phantom

According to local laws and regulations, no ethical approval was required for this prospective, experimental phantom study (no human subjects or animals were involved).

The study was performed by using 4 identically shaped rods made of the most commonly used prosthetic materials, including stainless steel (SS, ferromagnetic), cobalt-chromium-molybdenum (CoCr 7142–0040, ferromagnetic), titanium (Ti 7142–0168, paramagnetic), and oxidized zirconium (oxZi 7142–0316, paramagnetic). These rods were manufactured by Smith & Nephew (London, United Kingdom) and characterized by indentations of different length along their longitudinal axis (Fig. 1). They were individually placed in the center of a plastic drum phantom (manufactured by Smith & Nephew) filled with a 0.1% copper sulfate solution, which shortens the relaxation time in comparison to pure water.

Received for publication October 26, 2016; and accepted for publication, after revision, December 13, 2016.

From the *Institute of Diagnostic and Interventional Radiology, University Hospital Zurich, University of Zurich; †Institute for Biomedical Engineering, University and ETH Zurich, Zurich; ‡Department of Radiology, Kantonsspital Muensterlingen, Muensterlingen; §University of Zurich, Zurich; and ||Department of Radiology, Hospital and University of Bern, Inselspital, Bern, Switzerland.

Conflicts of interest and sources of funding: There was no financial support from the industry for this study. However, the metal rods used for this study were designed by Smith & Nephew. Philips Healthcare provided a "work-in-progress" software package for their scanner. Both companies had no influence on this study and did not receive any data or results. The authors had full control of the data at all time.

Nadja A. Farshad-Amacker has received grant support from the University of Zurich, Switzerland.

Correspondence to: Lukas Filli, MD, Institute of Diagnostic and Interventional Radiology, University Hospital Zurich, University of Zurich, Raemistrasse 100, 8091 Zurich, Switzerland. E-mail: lukas.filli@usz.ch.

ISSN: 0020-9996/17/5206–0381
DOI: 10.1097/RLI.0000000000000351

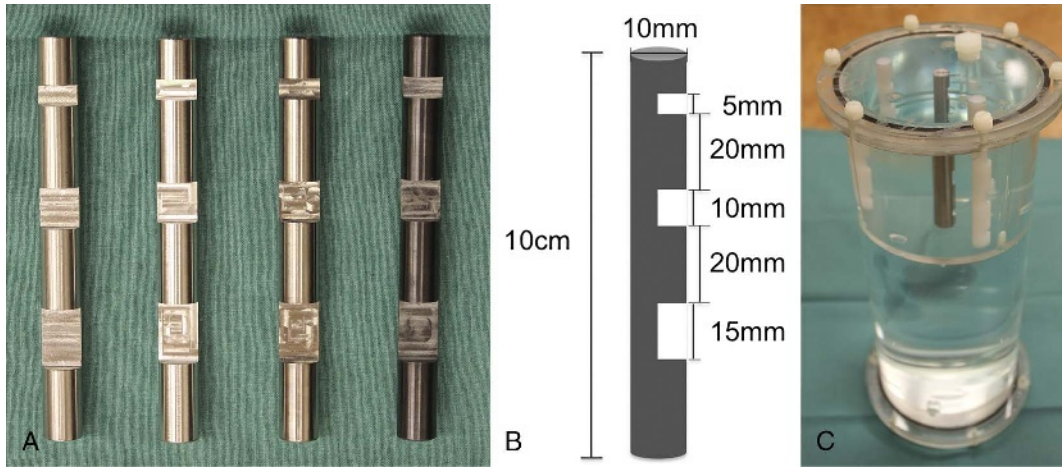

FIGURE 1. Illustration of the phantom. A, Identically shaped rods made of stainless steel, cobalt-chromium-molybdenum, titanium, and oxidized zirconium, respectively (from left to right). B, Rod geometry and dimensions of the 3 different indentations. C, Rod placed in the center of the plastic drum phantom filled with copper sulfate solution.

Magnetic Resonance Imaging

Magnetic resonance imaging was performed on a 3 T scanner (Ingenia; Philips Healthcare, Best, the Netherlands) using an 8-channel knee coil. Each rod was individually scanned. The rods were aligned within the plastic drum in the *z*-axis of the scanner (direction of the main magnetic field B0). Conventional fast spin-echo (FSE) images were acquired with 3 different image contrast weightings (T1w, T2w, PDw) with a predefined bandwidth of 291 Hz/pixel. In addition, metal artifact reduction sequences (SEMAC-VAT and MAVRIC) were applied with each of these weightings.

SEMAC-VAT and MAVRIC were part of a vendor-specific "work-in-progress" (WIP) software package. SEMAC-VAT was performed with different parameter settings predefined by the vendor: "weak," 7 slice-encoding steps; "medium," 15 slice-encoding steps; and "strong," 26 slice-encoding steps. Similarly, the MAVRIC sequences were performed at 3 different modes: "weak," 11 different off-resonance frequencies; "medium," 21 different off-resonance frequencies; and "strong," 31 different off-resonance frequencies. All scan parameters are summarized in Table 1.

Artifact Measurements

All measurements were performed using OSIRIX (v5.0.2; Pixmeo SARL, Bernex, Switzerland). Binary black-and-white images were generated by placing a region of interest (area, 1 cm^2) in the background noise (outside the phantom) and using its mean signal intensity divided by 3 to set the window level, while the window width was set to zero. For each rod and sequence, artifacts were measured on a single slice containing the center of the rod, where artifacts were most prominent. Two independent readers (L.F. and L.J.) measured artifacts as follows:

- Maximum in-plane artifacts = artifact caliber-thickness measured (millimeter) − 10 mm (thickness of the rod)
- Minimum in-plane artifact = artifact caliber-thickness measured (millimeter) − 5 mm (thickness of the rod at the level of indentations)
- Artifacts in frequency-encoding direction = real dimension of longest indentation (15 mm) − remaining visibility of the indentation (millimeter).
- Maximum through-plane artifacts = through-plane artifact caliber-thickness measured (millimeter) − 10 mm (thickness of the rod)
- Minimum through-plane artifacts = through-plane artifact caliber-thickness measured (millimeter) − 5 mm (thickness of the rod at the height of the indentations)
- Through-plane midline shift distortion artifacts = middle point of 2 points with the maximum midline distortion toward the right (millimeter) − middle point of 2 points with maximum distortion toward the left (millimeter).

Simulation

A digital 3-dimensional model reflecting the rod geometry embedded in a homogeneous environment with a 10 ppm lower magnetic susceptibility was generated with an isotropic resolution of 0.35 mm. The distribution of magnetic field offsets was calculated for a rod-orientation with a homogeneous magnetic field of 3 T aligned along its long axis, by convolution of the distribution of susceptibility differences, $\Delta\chi$, with the corresponding dipolar kernel, g:

$$\Delta B_0 = FT^{-1}(FT(\Delta\chi) \times g) \quad [1]$$

where FT and FT^{-1} denote the forward and inverse Fourier transformation, respectively, and with g, in Fourier, space being defined as:

$$g = \frac{1}{3} - \frac{k_z^2}{k^2}, \text{ with } k^2 = {}_x^2 + {}_y^2 + {}_z^2 \quad [2]$$

The relative field offsets ΔB_0 (in parts per billion), were scaled to absolute frequency offsets, $\Delta\nu$, using the proton gyromagnetic ratio and the field strength of 3 T. From the frequency-offset maps, maps of the frequency-offset gradient along the 3 orthogonal directions were calculated. Frequency-offset and frequency-offset-gradient (FOG) maps were then regridded to match the experimental in- and through-plane image resolution (nominal voxel diameters) for calculation of corresponding $\Delta\nu$ maps. The regridded FOG maps were scaled with the experimental voxel dimensions to obtain the bandwidths of resonance frequencies, $\Delta\Delta\nu_{frequency}$, $\Delta\Delta\nu_{phase}$, and $\Delta\Delta\nu_{slice}$ for crossing a voxel along the frequency-encoding, phase-encoding, and slice directions, respectively. As a measure of total resonance-frequency spread within a voxel, $\Delta\Delta\nu_{magn}$, was calculated as follows:

$$\Delta\Delta\nu_{magn} = \sqrt{\left(\Delta\Delta\nu_{frequency}\right)^2 + \left(\Delta\Delta\nu_{phase}\right)^2 + \left(\Delta\Delta\nu_{magn}\right)^2} \quad [3]$$

Statistical Analysis

Statistical analysis was performed using SPSS Statistics (v22.0.0.0; IBM, Somers, NY), and graphs were created with PRISM

TABLE 1. Imaging Parameters of the Different Sequences

	Conventional FSE			SEMAC-VAT			MAVRIC		
	T1w	T2w	PDw	T1w	T2w	PDw	T1w	T2w	PDw
TR, ms	510	4800	3500	510	4819	3500	428	2000	2000
TE, ms	27	40	27	27	63	27	27	62	27
Slice thickness, mm	3	3	3	3	3	3	3	3	3
No. slices	32	32	32	32	32	32	32	32	32
NEX	2	2	2	1	1	1	1	1	1
ETL	6	17	19	6	30	14	8	21	18
Bandwidth, Hz pixel^{-1}	291	290	293	665	665	665	665	665	665
FOV, mm × mm	160 × 160	160 × 160	160 × 160	160 × 160	160 × 160	160 × 160	160 × 160	160 × 160	160 × 160
Matrix	228 × 170	228 × 170	228 × 170	228 × 170	228 × 170	228 × 170	228 × 170	228 × 170	228 × 170
Flip angle, degree	90	90	90	90	90	90	90	90	90
Acquisition time, mins, weak/medium/strong	2:52	2:53	2:52	3:35/8:36/13:24	4:01/9:14/14:02	2:31/6:12/9:37	7:54/13:49/21:34 ("strong" not acquired)	12:16/14:10/18:54	14:16/14:24/15:18

FSE indicates fast spin echo; SEMAC, slice encoding for metal artifact correction; VAT, view angle tilting; MAVRIC, multiacquisition variable resonance image combination; TR, repetition time; TE, echo time; NEX, number of excitations; ETL, echo train length; FOV, field of view.

(v6; GraphPad, La Jolla, CA). Interobserver agreement was analyzed using intraclass correlation coefficients (ICCs). Intraclass correlation coefficients were interpreted according to Landis and Koch.[20]

RESULTS

Interobserver Agreement

The interobserver agreement of the measurements between the 2 readers was almost perfect for all measurements (ICC, 0.86–0.99), specifically for in-plane artifact measurements (ICC, 0.98–0.99), through-plane artifact measurements (ICC, 0.95–0.97) and midline shift distortion artifacts (ICC, 0.86).

Measured Artifact Dimensions

Stainless steel caused the greatest artifacts, followed by CoCr, Ti, and oxZi regardless of the applied sequence and image-contrast weighting (Figs. 2, 3). Different observations were made for individual types of artifacts as follows:

- In-plane, phase-encoding direction: In general, the weak SEMAC-VAT did not relevantly reduce, but sometimes even increase, the maximum artifact diameter compared with the FSE sequence. With "medium" and "strong" SEMAC-VAT or MAVRIC mode, the artifacts of SS and CoCr were relevantly reduced. In Ti and oxZi, the artifacts were already small with FSE such that a relevant reduction of artifact diameters was not noted with SEMAC-VAT or MAVRIC. However, signal loss artifacts were normalized with SEMAC-VAT and MAVRIC already when using the "weak" mode.
- In-plane, frequency-encoding direction: The artifact dimensions for SS and CoCr were similar with all sequences. However, for Ti and oxZi, the artifact dimensions were relevantly reduced using SEMAC-VAT and MAVRIC, most often already with the "weak" mode.
- Through-plane artifact reduction: The maximum diameters of through-plane artifacts were again relevantly reduced using higher SEMAC modes or MAVRIC, while the "weak" SEMAC mode showed no advantage or even an increase in artifact diameter, similar to the maximum in-plane artifacts in phase-encoding direction. In addition, the maximum artifact diameter in Ti and oxZi was again not further reduced as the artifacts were already very small using the FSE sequence. The minimum artifact diameter was again similar on all sequences with no additional advantage using the metal artifact reduction techniques. Midline shift distortion artifacts were relevantly reduced with SEMAC-VAT and MAVRIC. In all different metal rods, artifact reduction was less efficient on T2w images.

Simulation

Regarding the comparison between the experimental images and the simulated frequency-offset and FOG maps, the volumes of near-total signal loss around the rods matched well with the apparent geometry of the simulated maps (Fig. 4).

DISCUSSION

This phantom study systematically evaluated the effectiveness of SEMAC-VAT and MAVRIC for metal artifact reduction at 3 T. The size of various types of artifacts was compared between different prosthetic materials and different contrast weightings. Earlier studies focused on qualitative assessment[21–23] or quantitative measurements[18,24–26] of metal artifact reduction with dedicated sequences. To our best knowledge, this is the first study comparing SEMAC-VAT and MAVRIC at 3 T. In line with the literature, artifacts in the present study were most severe in case of SS, followed by CoCr, Ti, and oxZi,[8,17–19] which can be explained with the different magnetic susceptibility of these materials.[8]

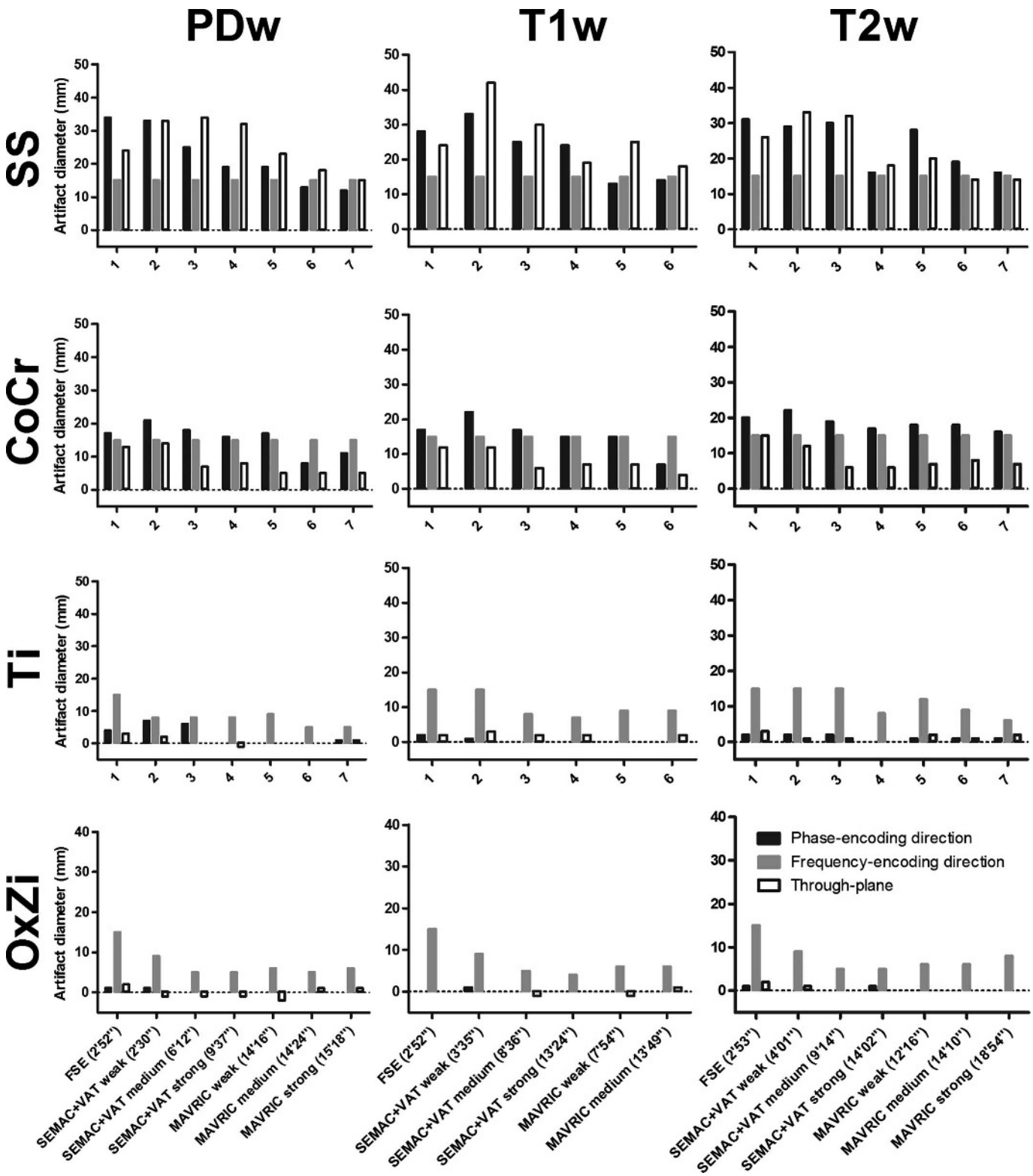

FIGURE 2. Maximum in-plane artifact diameters (millimeter) in phase-encoding and frequency-encoding direction as well as through plane-artifact diameters (millimeter) for the different measurements. The rods were made of 4 different prosthetic materials and were scanned at different contrast weightings (T1w, T2w, PDw) using conventional FSE as well as metal-artifact reduction sequences (SEMAC-VAT and MAVRIC) with different strength presets (weak, medium, and strong; see text). Acquisition times (in minutes ['] and seconds ["]) are shown as part of the sequence identification.

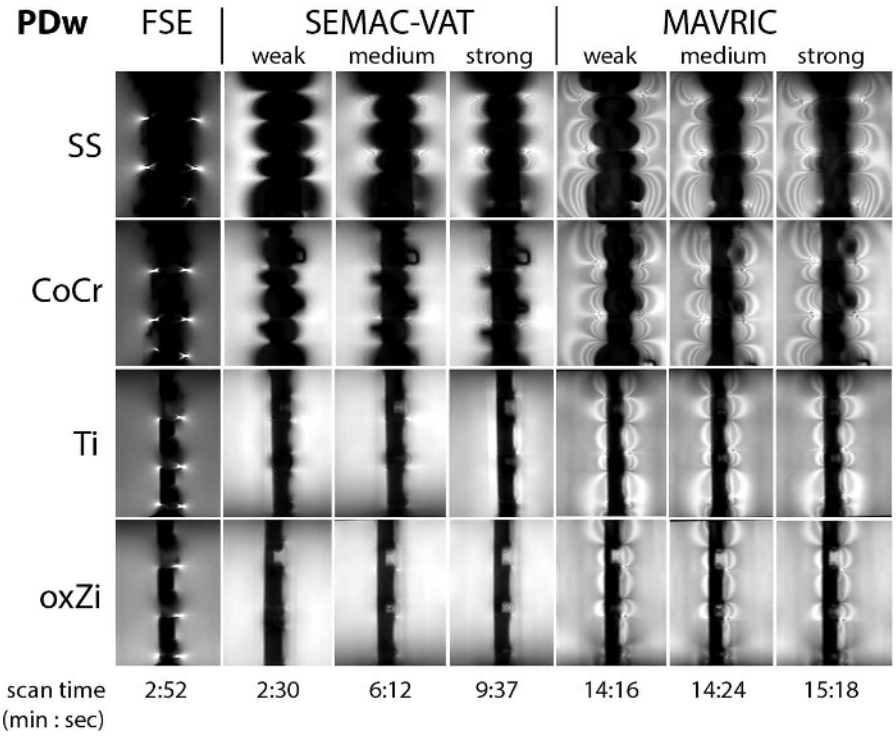

FIGURE 3. Proton density-weighted (PDw) images with susceptibility artifacts around different metallic rods using different presets of SEMAC-VAT (weak, medium, and strong: 7, 15, and 26 slice-encoding steps, respectively) and MAVRIC (weak, medium, and strong: 11, 21, and 31 different off-resonance frequencies, respectively) and corresponding acquisition times. SS, stainless steel; CoCr, cobalt-chromium-molybdenum; Ti, titanium; oxZi, oxidized zirconium.

Weak SEMAC-VAT (7 steps) did not relevantly reduce in-plane artifacts in the phase encoding direction compared with the conventional FSE sequence; in contrast, the artifact dimensions were often even larger. This seems reasonable, as the weak SEMAC-VAT mode needs even less scanning time than the FSE sequence. Indeed, effective artifact correction was reported with 11 and 15 slice-encoding steps, respectively,[23,25] whereas there is no study reporting effective artifact reduction with 7 steps. However, the weak SEMAC-VAT mode showed some advantage when scanning Ti and oxZi prosthesis, as signal loss artifacts and artifacts in frequency-encoding direction were reduced.

Through-plane artifacts were relevantly reduced using medium and high SEMAC-VAT modes or MAVRIC except for Ti and oxZi, where artifacts were already very small using FSE. Through-plane midline distortion artifacts were relevantly reduced using SEMAC-VAT and MAVRIC for all materials.

To verify the findings of the phantom measurements, simulations were performed. These showed that the measurements matched well with the apparent geometry of the frequency-offset maps, indicating that the performance of the sequences is critically dependent on the range of excited offset frequencies with the various techniques. In contrast, intravoxel dephasing does seem to be adequately refocused by the sequences, that is, excited spins seem typically also to be inverted by the FSE refocusing pulses, so that the geometries of near-total signal loss volumes do not resemble those with large frequency-offset gradients.

Based on the results of this study, the following general recommendations for optimal sequences (based on implant materials, contrast weightings and scan times) are made:

- SEMAC-VAT might be generally preferred over MAVRIC given its shorter scan times.
- SS: For T1w and PDw sequences, medium to strong SEMAC-VAT and medium MAVRIC seem reasonable sequences. For T2w sequences, strong SEMAC-VAT or medium to strong MAVRIC may be used.
- CoCr: Medium SEMAC-VAT or medium MAVRIC should be used, while MAVRIC adds some further artifact reduction at the cost of longer scan time.
- Ti and oxZi: Weak SEMAC-VAT might be preferred as this sequence was even faster (2 minutes, 30 seconds) than the FSE sequence (3 minutes), reduced the signal loss artifacts noted in FSE sequences in phase-encoding direction and relevantly reduced artifacts in frequency-encoding direction and through-plane distortion artifacts (Figs. 2, 3).

Both SEMAC-VAT and MAVRIC are limited by long scan times compared with conventional FSE. However, recent technical advances may overcome this limitation in the near future. In particular, compressed sensing has been successfully implemented for SEMAC of total hip and knee arthroplasties and allows a substantial reduction of scan times.[27–29] Advanced parallel imaging techniques such as CAIPIRINHA (controlled aliasing in parallel imaging results in higher acceleration) will further accelerate image acquisition and thus increase the clinical applicability of metal artifact reduction sequences.[30–32]

There are several limitations to the present study. First, the SEMAC-VAT and MAVRIC sequences on the 3 T Philips scanner were vendor-specific "WIP" software packages, which may be further changed for the final product release. An unusual observation is the occurrence of ringing artifacts around the metal rods with MAVRIC, the occurrence of which is still under investigation by the vendor. Second, no measurements at 1.5 T were included, because several studies already exist comparing metal artifact reduction at 1.5 T,[8,10,18,25] and the application of SEMAC-VAT and MAVRIC is most interesting at 3 T, where metal artifacts are more pronounced and general measures for artifact reduction (such as increasing the bandwidth or decreasing

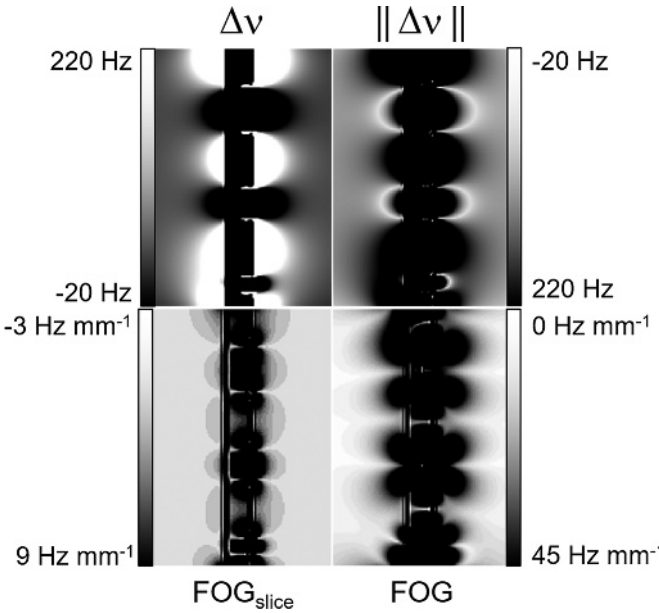

FIGURE 4. Maps of simulated distributions of (A) hypothetical proton-resonance frequency offset (Δν), (B) absolute value of the resonance-frequency offset (||Δν||), (C) through-slice bandwidth of frequency offsets (FOG_{slice}), and (D) the magnitude of the bandwidth components of frequency offsets along 3 orthogonal directions (FOG). Note that the grayscale for panels B, C, and D was inverted to facilitate visual comparison of zones with total signal loss in the example images with areas of large frequency offsets (B) that potentially are not excited by selective excitation pulses, and with areas of large frequency gradients (C, D) that potentially caused strong intravoxel dephasing. The simulation assumed the rod to have a higher magnetic susceptibility than its surroundings by an arbitrary amount of 10 ppm and a magnetic field strength of 3 T.

the voxel size) seem not sufficient in many clinical scenarios. Third, only descriptive statistics were used, as the amount of metal artifacts largely depend on the dimension and shape of the prosthetic material, and do not linearly increase with the size of the prosthesis. Still, the different effectiveness of SEMAC-VAT and MAVRIC depending on materials and image contrasts may apply regardless of the geometry of the prosthesis. Only signal void artifact dimensions were measured, whereas pileup artifacts were not detected; however, signal void-artifact cause the most relevant artifacts. Thus, we think that this is not a major limitation of our study.

Fourth, the acquisition times in this study need careful interpretation, because only the conventional sequences were acquired with 2 signal averages. This explains the shorter scan time of "weak" SEMAC compared with conventional FSE. However, no significant influence of different numbers of signal averages on metal artifacts is expected. Fifth, in-plane artifacts cannot be completely separated from through-plane artifacts, as some in-plane artifacts result from through-plane artifacts.[18] This explains the dependency of in-plane artifacts from the slice-encoding steps in SEMAC-VAT.

Last, the metal rods were only aligned along the *z*-axis of the scanner. However, it is usually possible in clinical routine to align the prosthetic material along the *z*-axis, and the effect of various angles on artifacts is already well studied.[17,33,34] Our general recommendations for parameter settings are based on artifacts around standardized rods; whether they are equally valid for various types of implants (eg, total hip or total knee arthroplasty) needs to be investigated in the future.

In conclusion, there is not 1 optimal scanning protocol for all implant materials. Metal artifact reduction techniques such as SEMAC-VAT and MAVRIC need to be tailored to the involved prosthetic material and the applied image contrast weighting.

REFERENCES

1. Wolford ML, Palso K, Bercovitz A. Hospitalization for total hip replacement among inpatients aged 45 and over: United States. *NCHS Data Brief*. 2000–2010; 2015:1–8.
2. Williams SN, Wolford ML, Bercovitz A. Hospitalization for total knee replacement among inpatients aged 45 and over: United States, 2000–2010. *NCHS Data Brief*. 2015;2015:1–8.
3. Chang EY, McAnally JL, Van Horne JR, et al. Metal-on-metal total hip arthroplasty: do symptoms correlate with MR imaging findings? *Radiology*. 2012;265:848–857.
4. Nawabi DH, Hayter CL, Su EP, et al. Magnetic resonance imaging findings in symptomatic versus asymptomatic subjects following metal-on-metal hip resurfacing arthroplasty. *J Bone Joint Surg Am*. 2013;95:895–902.
5. Hayter CL, Potter HG, Su EP. Imaging of metal-on-metal hip resurfacing. *Orthop Clin North Am*. 2011;42:195–205.
6. Fritz J, Lurie B, Miller TT, et al. MR imaging of hip arthroplasty implants. *Radiographics*. 2014;34:E106–E132.
7. Olsen RV, Munk PL, Lee MJ, et al. Metal artifact reduction sequence: early clinical applications. *Radiographics*. 2000;20:699–712.
8. Matsuura H, Inoue T, Ogasawara K, et al. Quantitative analysis of magnetic resonance imaging susceptibility artifacts caused by neurosurgical biomaterials: comparison of 0.5, 1.5, and 3.0 Tesla magnetic fields. *Neurol Med Chir (Tokyo)*. 2005;45:395–398. discussion 398–399.
9. Cho ZH, Kim DJ, Kim YK. Total inhomogeneity correction including chemical shifts and susceptibility by view angle tilting. *Med Phys*. 1988;15:7–11.
10. Ai T, Padua A, Goerner F, et al. SEMAC-VAT and MSVAT-SPACE sequence strategies for metal artifact reduction in 1.5T magnetic resonance imaging. *Invest Radiol*. 2012;47:267–276.
11. Sutter R, Ulbrich EJ, Jellus V, et al. Reduction of metal artifacts in patients with total hip arthroplasty with slice-encoding metal artifact correction and view-angle tilting MR imaging. *Radiology*. 2012;265:204–214.
12. Lu W, Pauly KB, Gold GE, et al. SEMAC: slice encoding for metal artifact correction in MRI. *Magn Reson Med*. 2009;62:66–76.
13. Agten CA, Del Grande F, Fucentese SF, et al. Unicompartmental knee arthroplasty MRI: impact of slice-encoding for metal artefact correction MRI on image quality, findings and therapy decision. *Eur Radiol*. 2015;25:2184–2193.
14. Koch KM, Lorbiecki JE, Hinks RS, et al. A multispectral three-dimensional acquisition technique for imaging near metal implants. *Magn Reson Med*. 2009;61: 381–390.
15. Koch KM, King KF, Carl M, et al. Imaging near metal: The impact of extreme static local field gradients on frequency encoding processes. *Magn Reson Med*. 2014;71:2024–2034. doi:10.1002/mrm.24862.
16. Koch KM, Brau AC, Chen W, et al. Imaging near metal with a MAVRIC-SEMAC hybrid. *Magn Reson Med*. 2011;65:71–82.
17. Harris CA, White LM. Metal artifact reduction in musculoskeletal magnetic resonance imaging. *Orthop Clin North Am*. 2006;37:349–359. vi.
18. Koff MF, Shah P, Koch KM, et al. Quantifying image distortion of orthopedic materials in magnetic resonance imaging. *J Magn Reson Imaging*. 2013;38:610–618.
19. Raphael B, Haims AH, Wu JS, et al. MRI comparison of periprosthetic structures around zirconium knee prostheses and cobalt chrome prostheses. *AJR Am J Roentgenol*. 2006;186:1771–1777.
20. Landis JR, Koch GG. The measurement of observer agreement for categorical data. *Biometrics*. 1977;33:159–174.
21. Chang SD, Lee MJ, Munk PL, et al. MRI of spinal hardware: comparison of conventional T1-weighted sequence with a new metal artifact reduction sequence. *Skeletal Radiol*. 2001;30:213–218.
22. Eustace S, Jara H, Goldberg R, et al. A comparison of conventional spin-echo and turbo spin-echo imaging of soft tissues adjacent to orthopedic hardware. *AJR Am J Roentgenol*. 1998;170:455–458.
23. Lee YH, Lim D, Kim E, et al. Usefulness of slice encoding for metal artifact correction (SEMAC) for reducing metallic artifacts in 3-T MRI. *Magn Reson Imaging*. 2013;31:703–706.
24. Lee MJ, Janzen DL, Munk PL, et al. Quantitative assessment of an MR technique for reducing metal artifact: application to spin-echo imaging in a phantom. *Skeletal Radiol*. 2001;30:398–401.
25. Reichert M, Ai T, Morelli JN, et al. Metal artefact reduction in MRI at both 1.5 and 3.0 T using slice encoding for metal artefact correction and view angle tilting. *Br J Radiol*. 2015;88:20140601.
26. Deligianni X, Bieri O, Elke R, et al. Optimization of scan time in MRI for total hip prostheses: SEMAC tailoring for prosthetic implants containing different types of metals. *RoFo*. 2015;187:1116–1122.

27. Fritz J, Fritz B, Thawait GK, et al. Advanced metal artifact reduction MRI of metal-on-metal hip resurfacing arthroplasty implants: compressed sensing acceleration enables the time-neutral use of SEMAC. *Skeletal Radiol*. 2016;45:1345–1356.
28. Fritz J, Ahlawat S, Demehri S, et al. Compressed sensing SEMAC: 8-fold accelerated high resolution metal artifact reduction MRI of cobalt-chromium knee arthroplasty implants. *Invest Radiol*. 2016;51:666–676.
29. Otazo R, Nittka M, Bruno M, et al. Sparse-SEMAC: rapid and improved SEMAC metal implant imaging using SPARSE-SENSE acceleration. *Magn Reson Med*. 2016. [Epub ahead of print].
30. Breuer FA, Blaimer M, Heidemann RM, et al. Controlled aliasing in parallel imaging results in higher acceleration (CAIPIRINHA) for multi-slice imaging. *Magn Reson Med*. 2005;53:684–691.
31. Filli L, Piccirelli M, Kenkel D, et al. Simultaneous multislice echo planar imaging with blipped controlled aliasing in parallel imaging results in higher acceleration: a promising technique for accelerated diffusion tensor imaging of skeletal muscle. *Invest Radiol*. 2015;50:456–463.
32. Fritz J, Fritz B, Thawait GG, et al. Three-dimensional CAIPIRINHA SPACE TSE for 5-minute high-resolution MRI of the knee. *Invest Radiol*. 2016;51:609–617.
33. Ganapathi M, Joseph G, Savage R, et al. MRI susceptibility artefacts related to scaphoid screws: the effect of screw type, screw orientation and imaging parameters. *J Hand Surg Br*. 2002;27:165–170.
34. Guermazi A, Miaux Y, Zaim S, et al. Metallic artefacts in MR imaging: effects of main field orientation and strength. *Clin Radiol*. 2003;58:322–328.